# Extraordinary refractive properties of photonic crystals of metallic nanorods

**Christos Tserkezis,[1,*] Nikolaos Stefanou,[1] and Nikolaos Papanikolaou[2]**

[1]*Section of Solid State Physics, University of Athens, Panepistimioupolis, GR-157 84 Athens, Greece*
[2]*Institute of Microelectronics, NCSR "Demokritos," GR-153 10 Athens, Greece*
[*]*Corresponding author: ctserk@phys.uoa.gr*

Received September 14, 2010; revised October 12, 2010; accepted October 14, 2010;
posted October 18, 2010 (Doc. ID 135062); published November 16, 2010

By applying a homogenization method based on systematic full-electrodynamic complex-band-structure calculations, we deduce the effective permittivity tensor of a uniaxial photonic crystal consisting of consecutive hexagonal arrays of aligned metallic nanorods of finite length. The form of the obtained permittivity tensor over a relatively broad low-frequency region, where homogenization is applicable, suggests the occurrence of unconventional refractive behavior, namely, negative refraction and self-collimation. This behavior is corroborated by straightforward calculation of the relevant group velocities in the actual photonic crystal. Moreover, it is shown that, in the frequency region where negative refraction occurs, a finite slab of the crystal possesses eigenmodes that form flat bands outside the light cone, as many as the number of its constituent layers. These eigenmodes allow for transfer of the evanescent components of an incident wave field to the other side of the slab, thus enabling subwavelength imaging. 

*OCIS codes:* 160.1190, 160.3918, 160.5293, 250.5403, 350.4238.

## 1. INTRODUCTION

The optical response of metallic nanorods has been extensively studied during the last years because of their unique properties associated with the excitation of different types of plasmonic modes. Because of their cylindrical shape, the threefold degeneracy of the predominant dipole plasmonic modes in a corresponding spherical particle [1] is lifted, and modes related to free-electron oscillations along either the long or the short axis of the nanorod can be observed [2–4]. These modes can be easily tuned within a broad frequency region by changing the geometrical characteristics, the dielectric environment, or the metallic material the nanorods are made of [5–9]. The situation becomes even more interesting when these particles are brought to interact with each other. Plasmon hybridization leads to much richer spectra in nanorod dimers or clusters [10–13], while arranging such particles periodically in space offers the possibility to combine plasmon tunability of the individual nanorods with controllable interparticle interaction [14–16]. Of particular interest are arrays of aligned nanorods arranged perpendicular to a substrate, because they are relatively easy to fabricate with chemical or lithographic methods [17–20] and can find numerous applications. For example, such arrays cause large enhancement of the electromagnetic (EM) field and are considered for surface enhanced Raman scattering [21]. Moreover, they are more sensitive to changes of the refractive index of the environment compared to isolated nanorods, thus becoming useful for biosensing applications [22]. When the nanorods approach each other, the EM field is concentrated in the interstitial region [18,23], and longitudinal standing waves are formed in the dielectric space between the rods [24], similarly to plasmonic cavity resonators. Taking advantage of their strongly anisotropic optical properties one can design polarization filters [25], while under certain conditions anisotropy results in negative refraction [26–28]. The use of nanorod arrays has also been considered as a possibility in the design of superlensing devices, since plasmons can travel through coupled metallic nanoparticles transferring near-field energy along the nanorods to relatively long distances, and then couple to conventional optics to generate the image [29]. In the same context, three-dimensional (3D) crystals of metallic nanorods were proposed to achieve both long propagation length and broadband operation toward color subwavelength imaging [30].

In this article we focus on the description of 3D photonic crystals of metallic nanorods as optical metamaterials and, in particular, their extraordinary optical properties such as negative refraction and wide-angle self collimation. A valuable tool in the study of metamaterials is the choice of a reliable homogenization method. Here we use a homogenization approach based on least-squares fits of dispersion data for the actual crystal obtained by full-electrodynamic calculations for many propagation directions to the corresponding analytic relations for a uniaxial homogeneous medium. All calculations are carried out by the extended layer-multiple-scattering (ELMS) method [31–33], which is ideally suited for the case under consideration. Besides the complex photonic band structure of the infinite crystal, the method allows one to calculate, also, the reflection and transmission coefficients of an EM wave incident at any angle either on a finite slab or on a semi-infinite crystal [34], and, in this respect, it can describe an actual transmission experiment. Another advantage of the method is that it solves Maxwell's equations in the frequency domain, and therefore it can treat

 

strongly dispersive materials such as metals and include losses, which always exist in real materials, in a straightforward manner. The properties of the individual scatterers enter only through the corresponding scattering $T$ matrix which, for homogeneous spherical particles, is given by the closed-form solutions of the Mie-scattering problem, while for scatterers of arbitrary shape it is calculated numerically by the extended-boundary-condition method [35]. At a first step, in-plane multiple scattering is evaluated in a spherical-wave basis using proper propagator functions. Subsequently, interlayer scattering is calculated in a plane-wave basis through appropriate reflection and transmission matrices. The scattering $S$ matrix of a multilayer slab, which transforms the incident into the outgoing wave field, is obtained by combining the reflection and transmission matrices of the component layers. The ratio of the transmitted or reflected energy flux to the energy flux associated with the incident wave defines the transmittance or reflectance of the slab, respectively. On the other hand, for a 3D crystal consisting of an infinite periodic sequence of layers stacked along the $z$ direction, applying the Bloch condition for the wave field in the region between two consecutive unit slabs leads to an eigenvalue equation that gives the $z$ component of the Bloch wave vector, $k_z$, for given frequency $\omega$ and in-plane reduced wave vector component $\mathbf{k}_\parallel$, which are conserved quantities in the scattering process. The eigenvalues $k_z(\omega,\mathbf{k}_\parallel)$, looked upon as functions of real $\omega$, define, for each $\mathbf{k}_\parallel$, lines (sometimes they are called real-frequency lines) in the complex $k_z$ plane. Taken together they constitute the complex band structure of the infinite crystal associated with the given crystallographic plane. A line of given $\mathbf{k}_\parallel$ may be real (in the sense that $k_z$ is real) over certain frequency regions and be complex (in the sense that $k_z$ is complex) for $\omega$ outside these regions. It turns out that for given $\mathbf{k}_\parallel$ and $\omega$, out of the eigenvalues $k_z(\omega,\mathbf{k}_\parallel)$, none or, at best, a few are real, and the corresponding eigenvectors represent propagating modes of the EM field in the given infinite crystal. The remaining eigenvalues $k_z(\omega,\mathbf{k}_\parallel)$ are complex and the corresponding eigenvectors represent evanescent waves. These have an amplitude that increases exponentially in the positive or negative $z$ direction and, unlike the propagating waves, do not exist as physical entities in the infinite crystal. However, they are an essential part of the physical solutions of the EM field in a slab of finite thickness. A region of frequency where propagating waves do not exist for given $\mathbf{k}_\parallel$ constitutes a frequency gap of the EM field for the given $\mathbf{k}_\parallel$. If over a frequency region no propagating wave exists whatever the value of $\mathbf{k}_\parallel$, then this region constitutes an absolute frequency gap. In order to ensure adequate convergence for the structure considered in the present work, we truncate the spherical-wave expansions at $\ell_{\max}=12$ and take into account 61 two-dimensional (2D) reciprocal lattice vectors in the relevant plane-wave expansions, while the single-particle scattering $T$ matrix is evaluated with $\ell_{\text{cut}}=16$ and a Gaussian quadrature integration formula with 4000 points [33,36].

The paper is organized as follows. In Section 2 we describe the geometry of the crystal under consideration and analyze its complex photonic band structure in the frequency region of interest. In Section 3 we apply our homogenization method and discuss the results in comparison with those of standard effective-medium theories. Subsequently, in Section 4 the unconventional refractive behavior anticipated from the form of the effective permittivity tensor is analyzed in conjunction with the corresponding group velocities deduced from rigorous calculation of the isofrequency surfaces of the actual crystal. Moreover, we discuss the role of bound states of the slab in the frequency region of interest in the transmission of the evanescent components of an incident wave field. Our results are summarized in the last section.

## 2. COMPLEX PHOTONIC BAND STRUCTURE

We consider an infinite 3D crystal built of consecutive layers parallel to the $x-y$ plane of identical, free-standing metallic nanorods aligned parallel to their long axis ($z$ direction). We assume that the metallic material is described by the Drude dielectric function [37]

$$\varepsilon_{\text{m}}(\omega)=1-\frac{\omega_{\text{p}}^2}{\omega(\omega+i\tau^{-1})}, \tag{1}$$

where $\omega_{\text{p}}$ is the bulk plasma frequency, and $\tau$ is the relaxation time of the conduction-band electrons of the metal. To begin with, we disregard absorptive losses assuming $\tau^{-1}=0$. The nanorods have a circular cross section, with diameter $D=c/\omega_{\text{p}}$ and height $H=2.5c/\omega_{\text{p}}$, parameters that yield fast convergence of the calculations and allow, at the same time, comparison with the results of other works [29,30]. We note that, assuming $\hbar\omega_{\text{p}}\cong 10$ eV, the diameter of the nanorods corresponds to about 20 nm and their height to about 50 nm. For longer nanorods such as those described in [17,18,24] the main difference expected is a redshift of the principal longitudinal mode [16]. The nanorods in each layer are arranged on a hexagonal lattice defined by the primitive vectors $\mathbf{a}_1=a(1,0,0)$ and $\mathbf{a}_2=a(1/2,\sqrt{3}/2,0)$, while adjacent planes of nanorods are displaced by $\mathbf{a}_3=a(0,0,1)$. Taking $a=3c/\omega_{\text{p}}$ ensures relatively strong interaction between the nanorods in each layer, while the main longitudinal and transverse modes are still well discernible [16]. A schematic view of the crystal under consideration is shown in Fig. 1.

The photonic band structure of the given crystal has been presented elsewhere [16], and its main characteristics can be summarized as follows. The symmetry of the bands along the [001] direction is that of the $C_{6v}$ group [38]. There is a linear doubly degenerate dispersion curve of $E_1$ symmetry, as expected for propagation in a homogeneous medium, up to $\omega=0.45\omega_{\text{p}}$. This band is crossed by an almost flat, non-degenerate band of $A_1$ symmetry about $\omega=0.36\omega_{\text{p}}$, which originates from particle-plasmon modes of the individual metallic nanorods, of mainly di-

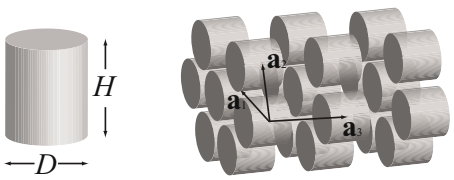


Fig. 1. Schematic view of the photonic crystal of metallic nanorods under consideration.

pole electric character, associated with electron oscillations along their long axis. Correspondingly, for $\mathbf{k}_\parallel=(k_x,0)$, $0<k_x<4\pi/3a$, i.e., along the $\overline{\Gamma\mathrm{K}}$ direction of the surface Brillouin zone (SBZ), the point group of the wave vector is the $C_{1h}$ group, and the electric field eigenmodes can be classified as even ($Q_1$) or odd ($Q_2$) upon reflection with respect to the $x-z$ plane. According to group theory, a doubly degenerate band of $E_1$ symmetry (for $\mathbf{k}_\parallel=\mathbf{0}$) splits for $\mathbf{k}_\parallel=(k_x,0)$ into one band of $Q_1$ and one of $Q_2$ symmetry; similarly, an $A_1$ band gives a $Q_1$ band. In our case, the $Q_1$ bands that originate from the $E_1$ and $A_1$ bands interact with each other and give rise to a resonance hybridization gap about the crossing point, as shown in Fig. 2. On the other hand, the $Q_2$ band clearly has the form of a linear, effective-medium band throughout the whole frequency region that we consider here, and therefore it is of no particular interest. In the region of the resonance gap where there are no propagating $Q_1$ modes, the $Q_1$ bands continue analytically in the complex $k_z$ plane [39]. In this region we show the dispersion lines for complex values of $k_z$ that correspond to the $Q_1$ bands with the smallest-in-magnitude imaginary part and that are, therefore, the ones that determine propagation of light in the given crystal.

A transverse magnetic (TM)- or transverse electric (TE)-polarized EM wave incident on a finite (001) slab of the given crystal with $\mathbf{k}_\parallel=(k_x,0)$ excites bands of $Q_1$ or $Q_2$ symmetry, respectively, and through them is transmitted to the other side of the slab. In Fig. 2, next to the photonic band structure we also show the corresponding reflectivity of a slab consisting of eight (001) layers, together with the reflectivity of the semi-infinite crystal. It can be seen that the reflectivity of the finite slab exhibits the well-known Fabry–Perot oscillations, with period $k_z a/\pi=1/8$. In the case of the semi-infinite crystal, since there is no rear surface to generate multiple reflections, these oscillations are absent. Within the gap, where the transmittance vanishes, the reflectance equals unity as expected in the absence of absorptive losses.

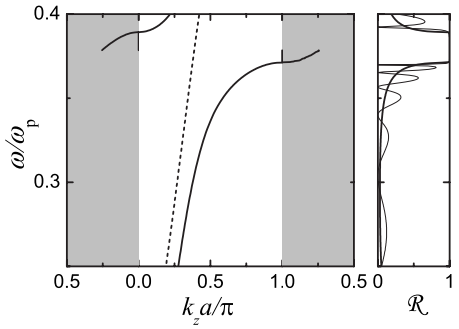


Fig. 2. Complex photonic band structure of the crystal shown in Fig. 1 for $\mathbf{k}_\parallel=(0.2\pi/a,0)$, neglecting absorptive losses. Solid (dashed) curves correspond to bands of $Q_1$ ($Q_2$) symmetry. The segments of the $Q_1$ complex bands with the smallest-in-magnitude imaginary part over the gap region are shown in gray-shaded areas. Next to the band diagram we display the reflectance for TM-polarized light impinging with $\mathbf{q}_\parallel=(0.2\pi/a,0)$ on a slab consisting of eight (001) layers of the given crystal (light curve) together with the reflectance of the corresponding semi-infinite crystal (heavy curve).

## 3. HOMOGENIZATION METHOD

Since the photonic crystal under consideration has uniaxial symmetry, at sufficiently long wavelengths it can be described by effective permittivity and permeability tensors. If we take the $z$ axis to be the optical axis, these tensors have the form [40]

$$\varepsilon=\begin{pmatrix}\varepsilon_1 & 0 & 0\\ 0 & \varepsilon_1 & 0\\ 0 & 0 & \varepsilon_z\end{pmatrix}, \tag{2}$$

$$\boldsymbol{\mu}=\begin{pmatrix}\mu_1 & 0 & 0\\ 0 & \mu_1 & 0\\ 0 & 0 & \mu_z\end{pmatrix}, \tag{3}$$

in the $(x,y,z)$ coordinate system. In the case we are examining here we can assume $\mu_1=\mu_z=1$ (see below). Therefore one has to determine only two EM parameters, the permittivity tensor components $\varepsilon_1$ and $\varepsilon_z$. These parameters can be evaluated numerically by an all-angle homogenization method based on systematic photonic-band-structure calculations for the actual crystal. We note that this method yields local effective parameters that describe the behavior of the given crystal for every propagation direction, contrary to other methods, e.g., the commonly used $S$-matrix retrieval procedure [41–43], that are usually limited to a specific propagation direction. Our method proceeds as follows.

A plane wave of angular frequency $\omega$ and wave vector $\mathbf{q}$ propagating in a homogeneous uniaxial medium obeys the dispersion relations

$$q_\parallel^2+q_{(\mathrm{TE})z}^2=\varepsilon_1\frac{\omega^2}{c^2}, \tag{4}$$

and

$$\frac{\varepsilon_1}{\varepsilon_z}q_\parallel^2+q_{(\mathrm{TM})z}^2=\varepsilon_1\frac{\omega^2}{c^2}, \tag{5}$$

for TE and TM polarizations, respectively, where $\mathbf{q}_\parallel=(q_x,q_y)$ is the wave-vector component normal to the optical axis. Through linear least-squares fits of dispersion data points, $(q_\parallel^2,q_z^2)$, calculated for the given photonic crystal by the ELMS method for the two polarization modes and many propagation directions, to Eqs. (4) and (5) looked upon as linear equations of $q_{(\mathrm{TE})z}^2$ or $q_{(\mathrm{TM})z}^2$ versus $q_\parallel^2$, we obtain two values for $\varepsilon_1$ from the constant terms of these equations as well as $\varepsilon_1/\varepsilon_z$ from the fit to Eq. (5). Taking the average of the two values for $\varepsilon_1$ we can then deduce $\varepsilon_z$ from the ratio $\varepsilon_1/\varepsilon_z$. The quality of the fits—a quantitative estimate of which can be given by the average standard deviation of the fitting procedure and the agreement of the values of $\varepsilon_1$ obtained independently from the two polarizations—provide strict criteria for the validity of the assumption of a homogeneous uniaxial medium and its description by the deduced set of local EM parameters. A similar homogenization procedure, which fits experimental data obtained for many angles of incidence to the dispersion Eqs. (4) and (5) has also been presented recently [44]. The variation of $\varepsilon_1$ and $\varepsilon_z$ versus fre-

quency obtained in the above manner is displayed in Fig. 3 by solid curves, together with the corresponding standard deviation. Inside the resonance gap the fitting procedure fails completely when the relevant band corresponds to $\mathrm{Re}\,k_z=1$ (complex coefficients in the dispersion equation), as expected [45,46], and we do not present the retrieved parameters (black-shaded region). However, when the relevant band corresponds to $\mathrm{Re}\,k_z=0$ (real coefficients in the dispersion relation), the fitting procedure works relatively well, and the results are shown in Fig. 3. The standard deviation of the fits is relatively large near the edge of the Brillouin zone as well, which implies that in this region the description of the crystal by local effective parameters is also questionable, as expected. We should also note at this point that we verified our assumption that $\mu_1=\mu_z=1$ by applying a recently reported full homogenization scheme [34] at a few characteristic frequencies.

It is interesting to compare our homogenization method with standard effective-medium theories. A frequently used approximation is to assume that the rods are infinite in length, and use 2D Maxwell–Garnett or Bruggeman theories [13,26]. These theories however naturally fail to predict the observed resonance in the $z$ component of the permittivity tensor, and thus we shall appeal to generalizations of the Maxwell–Garnett theory that take into account the finite length of the nanorods [47]. In this case it is the particle aspect ratio, rather than its exact geometry, that is relevant. It is therefore convenient to approximate the cylinders with ellipsoids, identical in shape and orientation, since the depolarization tensor of the ellipsoid is analytically known [48]:

$$L_z=\frac{1-e^2}{e^2}\left[\frac{1}{2e}\ln\left(\frac{1+e}{1-e}\right)-1\right],$$

$$L_x=L_y=\frac{1-L_z}{2}, \tag{6}$$

where $e^2=(1-D^2/H^2)$. The effective permittivity, $\varepsilon_{\mathrm{eff}}$, of a system of metallic ellipsoids described by a permittivity $\varepsilon_{\mathrm{m}}$ embedded in a dielectric medium of permittivity $\varepsilon_{\mathrm{h}}$ is given by [49]

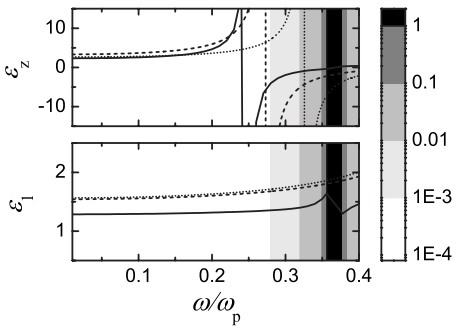


Fig. 3. Effective permittivities $\varepsilon_z$ and $\varepsilon_1$ of the photonic crystal shown in Fig. 1 calculated by least-squares fits of dispersion data, obtained for many propagation directions, to Eqs. (4) and (5) (solid curves). The standard deviation of the fitting procedure is shown by gray-shaded areas. Corresponding results of the effective-medium approximations of Eqs. (7) and (8) are represented by dashed and dotted curves, respectively.

$$\frac{\varepsilon_{\mathrm{eff}(i)}-\varepsilon_{\mathrm{h}}}{\varepsilon_{\mathrm{eff}(i)}+2\varepsilon_{\mathrm{h}}}=\frac{f}{3}\frac{\varepsilon_{\mathrm{m}}-\varepsilon_{\mathrm{h}}}{\varepsilon_{\mathrm{h}}+L_i(\varepsilon_{\mathrm{m}}-\varepsilon_{\mathrm{h}})}, \tag{7}$$

where the index $i$ denotes the axis, $x$, $y$, or $z$, and $f$ is the volume filling fraction. This formula has been successfully used to describe thin films comprising gold nanorods embedded in an alumina matrix [17]. On the other hand, it has been shown that Eq. (7) leads to inconsistencies when $L_i\simeq 0$ or $L_i\simeq 1$, and the following alternative form has been proposed [50]:

$$\frac{\varepsilon_{\mathrm{eff}(i)}-\varepsilon_{\mathrm{h}}}{\varepsilon_{\mathrm{h}}+L_i(\varepsilon_{\mathrm{eff}}-\varepsilon_{\mathrm{h}})}=f\frac{\varepsilon_{\mathrm{m}}-\varepsilon_{\mathrm{h}}}{\varepsilon_{\mathrm{h}}+L_i(\varepsilon_{\mathrm{m}}-\varepsilon_{\mathrm{h}})}. \tag{8}$$

The effective permittivities obtained through Eqs. (7) and (8) are presented in Fig. 3 with dashed and dotted curves, respectively. In our case the depolarization factor associated with the $z$ axis, $L_z$, is 0.14, while $L_x=L_y=0.43$. As can be seen in Fig. 3, Eq. (7) gives results closer to those of our homogenization method than Eq. (8). However, the above effective-medium theories do not take into account the exact geometry of the system, and more elaborated models, such as the retarded-dipole-interaction model [51], are expected to yield better agreement with the results of the exact calculations.

## 4. EXTRAORDINARY REFRACTIVE PROPERTIES

The most prominent feature of the effective permittivities shown in Fig. 3 is a resonance of $\varepsilon_z$ in the frequency region about $0.25\omega_{\mathrm{p}}$. In this region, $\varepsilon_z$ first increases asymptotically and then takes negative values up to the gap, while $\varepsilon_1$ is positive and varies very slowly. Such media, in which not all constitutive-tensor components have the same sign, are termed indefinite [52] and have been proven to support backward waves [53,54]. Although at $\omega\cong 0.3\omega_{\mathrm{p}}$ the vacuum wavelength is only about 7 times greater than the lattice constant, homogenization yields local effective parameters with a standard deviation in the fitting procedure smaller than 1%. Even though homogenization in this region is not as good as at lower frequencies, the unconventional refractive behavior anticipated from the obtained effective parameters is confirmed through rigorous full-electrodynamic calculations.

Because of the uniaxial symmetry of the crystal under consideration we can assume, without loss of generality, that $k_y=0$ and consider the much easier to handle 2D isofrequency lines instead of the corresponding 3D surfaces. Figure 4 displays isofrequency contours, $\omega(\mathbf{k})=const.$, in the $k_x-k_z$ plane, for modes of $Q_1$ symmetry in the frequency region between $0.15\omega_{\mathrm{p}}$ and $0.35\omega_{\mathrm{p}}$. One clearly sees from the figure that, as the frequency increases and approaches the region where the homogenization procedure gives negative $\varepsilon_z$, the isofrequency contours are gradually transformed from ellipses to straight lines and then to hyperbolas. The full 3D isofrequency surfaces inside the first Brillouin zone at $\omega=0.30\omega_{\mathrm{p}}$ are shown in Fig. 5 for completeness. The one is almost spherical, as expected from Eq. (4) for a medium with positive $\varepsilon_1$, and the other looks like a hyperboloid, as expected from Eq. (5) for a medium with positive $\varepsilon_1$ and negative $\varepsilon_z$. The

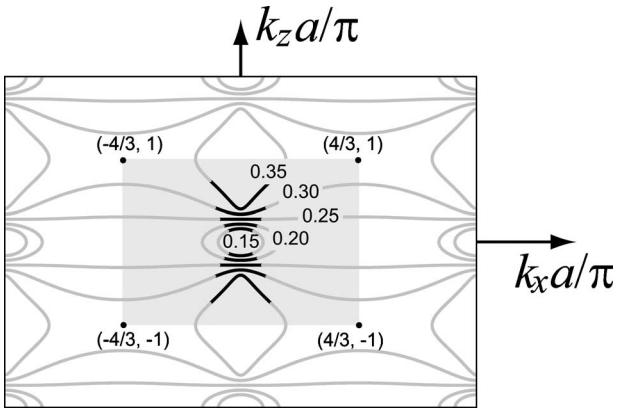


Fig. 4. Isofrequency contours in the $k_x-k_z$ plane ($k_y=0$), associated with the $Q_1$ modes at different frequencies (in $\omega_p$ units). The shaded rectangle shows the projection of the first Brillouin zone on this plane. Only the heavy segments of the contours correspond to propagating waves outside the crystal.

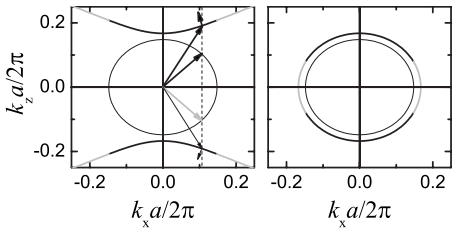


Fig. 6. Wave-vector diagrams in the $k_x-k_z$ plane ($k_y=0$) corresponding to $Q_1$ (left-hand panel) and $Q_2$ (right-hand panel) modes at $\omega=0.30\omega_p$ for the crystal of Fig. 1. The light circles are the isofrequency curves in air, while the hyperbola (left-hand panel) and the heavy circle (right-hand panel) are the corresponding curves in the photonic crystal. The dashed vertical line is the construction line. Long arrows represent wave vectors in the different media, and short arrows normal to the isofrequency curves represent the group velocity of the transmitted wave. Thin black arrows in the negative $k_z$ plane indicate the wave vector and group velocity of a transmitted wave for which the $k_x$ component is conserved but causality is violated.

light-gray parts of these isofrequency surfaces extend over regions of $\mathbf{k}_\parallel$ that correspond to evanescent waves in the embedding medium (air).

In order to better understand the physical meaning of the isofrequency surfaces presented above, we analyze corresponding cross sections of such characteristic surfaces for $k_y=0$, for two frequencies of particular interest: $\omega=0.30\omega_p$ (Fig. 6) and $\omega=0.25\omega_p$ (Fig. 7). Since, as discussed before, the $Q_2$ modes, which can be excited by a TE incident wave, are not of particular interest, we restrict our analysis to the $Q_1$ modes, which can be excited by a TM incident wave. When light impinges on the $x-y$ surface of the crystal with $\mathbf{q}_\parallel=\mathbf{k}_\parallel=(k_x,0)$, the wave-vector component parallel to the surface ($k_x$) is conserved. In Figs. 6 and 7 this condition is provided by the vertical (dashed) construction line. Its intersection with the isofrequency curve in air (the thin circle) determines the reflected wave, while its intersection with the corresponding isofrequency curves of the uniaxial crystal (the hyperbola in Fig. 6 and the straight lines in Fig. 7) provides two possible wave vectors for the transmitted wave. In order to determine which one corresponds to the actual transmitted wave, we have to consider the direction of the group velocity, $\mathbf{v}_g\equiv\nabla_{\mathbf{k}}\omega(\mathbf{k})$. The group velocity specifies the direction of energy flow for the wave. It is not necessarily parallel to the wave vector but it must be normal to the isofrequency surface. Calculation of $\mathbf{v}_g$ determines which of the two possible normal directions yields increasing $\omega$ and is therefore the correct group velocity direction (see also Fig. 4). Moreover, the transmitted wave must be pointing away from the interface, i.e., it must have a positive $z$ component of $\mathbf{v}_g$ [55,56]. Thus, in Fig. 6 we choose the transmitted wave to be the one with negative $x$ component of $\mathbf{v}_g$. In other words, the photonic crystal under consideration exhibits negative refraction for TM incident waves (and positive, regular refraction for TE incident waves) at $\omega=0.30\omega_p$. At $\omega=0.25\omega_p$, as expected from the calculated effective permittivity shown in Fig. 3, $\varepsilon_z$ diverges asymptotically and the corresponding isofrequency line is flat for all values of $k_x$ appropriate to an externally incident wave (see also Fig. 4). This implies that, in this case, at any angle of incidence, the group velocity and thus the energy flow of the transmitted wave will be directed along the same direction, namely the $z$ direction. This phenomenon, so called self-collimation [57], has already been reported for 2D and 3D dielectric photonic crystals [58–60], and can be useful in the design of integrated optics circuits and other applications [61].

In order for a photonic crystal slab to be enabled for subwavelength imaging, it has to be able to transfer without attenuation evanescent waves as well. This can be achieved, in general, through flat surface or slab modes, if such exist, in the frequency region where negative refraction occurs [62]. In Fig. 8 we present the projection of the photonic band structure of the crystal under consideration on the symmetry lines of the SBZ of its (001) surface. The shaded regions extend over the frequency bands of the EM field: at any one frequency within a shaded region, for given $\mathbf{k}_\parallel$, there exists at least one propagating

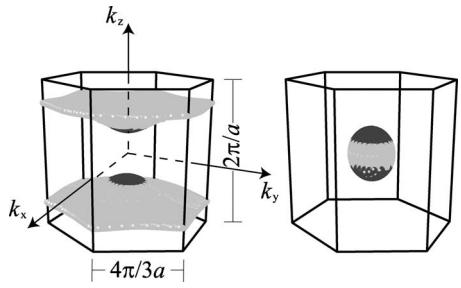


Fig. 5. Calculated isofrequency surfaces of the photonic crystal of Fig. 1 at $\omega=0.30\omega_p$ associated with the TM-like (left-hand panel) and TE-like (right-hand panel) modes inside the first Brillouin zone.

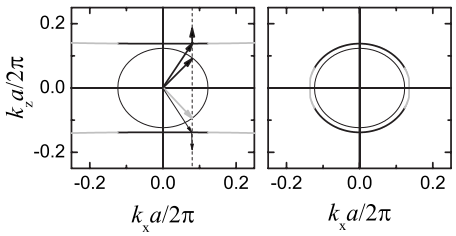


Fig. 7. Same as in Fig. 6 at $\omega=0.25\omega_p$.

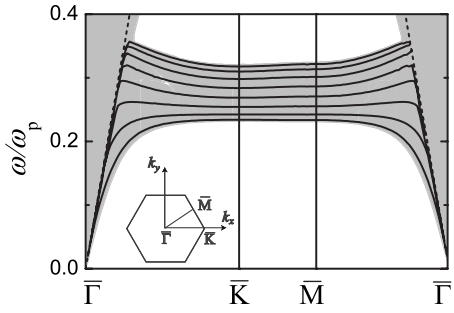


Fig. 8. Projection of the photonic band structure of the crystal of Fig. 1 on the SBZ of its (001) surface along the symmetry lines shown in the inset. With heavy curves we present the eigenmodes of an eight-layer-thick slab of the above crystal. The dotted lines show the light cone in air.

EM mode in the infinite crystal. The blank regions represent frequency gaps for the given $\mathbf{k}_\parallel$. Obviously an absolute gap exists only when a blank region of frequency is common to all $\mathbf{k}_\parallel$. We note that knowing the modes with $\mathbf{k}_\parallel$ in the $\overline{\Gamma KM}$ triangle of the SBZ shown in the inset of Fig. 8 and $0 \leqslant k_z \leqslant \pi/a$ is sufficient for a complete description of all the modes in the infinite crystal. The modes in the remaining of the reduced $\mathbf{k}$ space are obtained through symmetry. In Fig. 8 we also show with solid curves the eigenmodes of a slab consisting of eight successive (001) layers of the given crystal, calculated by the ELMS method, while the dashed lines denote the light cone. As can be seen from the figure, and we also verified numerically for various slab thicknesses, there appear several flat bands outside the light cone, as many as the number of layers. These correspond to slab modes and are accompanied by a significant increase in the relevant transmission matrix element, as Luo *et al.* [62] discussed and we also verified. They originate from an interaction between corresponding bound states of the EM field localized about consecutive (001) layers of the given crystal. For every $\mathbf{k}_\parallel$ the eigenfrequencies of a slab comprising $N_L$ layers plotted against values of the reduced wave number $k_z = \kappa\pi/(N_L+1)a$, $\kappa = 1, 2, \ldots, N_L$, reproduce the corresponding dispersion curves of the infinite crystal [16]. As the number of layers increases, these slab modes increase accordingly and come closer to each other, covering the corresponding gray-shaded area of Fig. 8. We note that, when dealing with the imaging of a source of monochromatic radiation, it is preferable for the lens to possess such flat slab modes near but not exactly at the operating frequency; otherwise the amplification of evanescent waves will be so intense that the picture will be blurred [62]. On the other hand, for color imaging one needs a large number of such modes, close to each other [30]. In any case, in the crystal under consideration, the number and frequency position of the flat slab modes can be tailored by appropriately adjusting the slab thickness.

So far we have neglected absorptive losses in the metallic material. The realistic complex permittivity of the metal can be introduced by setting $\tau^{-1} \neq 0$ in Eq. (1). This causes all bands to become complex, in the sense that all values of the wave vector acquire a small imaginary part to account for dissipative losses. Taking $\tau^{-1} \cong 0.01\omega_p$, which is appropriate for gold, the imaginary part of $k_z a/\pi$ for the relevant bands is always smaller than 0.04. This implies a propagation length longer than 8 lattice constants along the propagation direction. On the other hand, for a low-loss metal like silver ($\tau^{-1} \cong 0.002\omega_p$), this propagation length may become as long as 30–40 lattice constants. This corroborates that finite slabs consisting of a few layers of 2D periodic arrays of metallic nanorods can be useful in practical applications related to unconventional refraction and imaging.

## 5. CONCLUSION

In summary, we employed a homogenization method based on rigorous full-electrodynamic calculations to describe the effective optical properties of a hexagonal photonic crystal of metallic nanorods. The homogenization procedure revealed the existence of a broad frequency region where extraordinary refractive phenomena, such as negative refraction and self-collimation, are expected for TM-polarized incident waves. This behavior was verified by calculating the isofrequency surfaces of the actual crystal at some characteristic frequencies and deriving the corresponding group velocities of the transmitted waves. Moreover we showed that finite slabs of the given crystal have the ability to transfer evanescent waves in the frequency region where negative refraction occurs over relatively long distances through flat bands of slab modes, thus enabling subwavelength imaging applications.

## ACKNOWLEDGMENTS

This work was supported by the research program "Kapodistrias" of the University of Athens.

## REFERENCES

1. N. Stefanou and A. Modinos, "Optical properties of thin discontinuous metal films," J. Phys.: Condens. Matter **3**, 8149–8157 (1991).
2. E. R. Encina and E. A. Coronado, "Plasmonic nanoantennas: angular scattering properties of multipole resonances in noble metal nanorods," J. Phys. Chem. C **112**, 9586–9594 (2008).
3. Y.-F. Chau, M. W. Chen, and D. P. Tsai, "Three-dimensional analysis of surface plasmon resonance modes on a gold nanorod," Appl. Opt. **48**, 617–622 (2009).
4. G. Gantzounis, "Plasmon modes in axisymmetric metallic nanoparticles: a group theory analysis," J. Phys. Chem. C **113**, 21560–21565 (2009).
5. K.-S. Lee and M. A. El-Sayed, "Dependence of the enhanced optical scattering efficiency relative to that of absorption for gold metal nanorods on aspect ratio, size, end-cap shape, and medium refractive index," J. Phys. Chem. B **109**, 20331–20338 (2005).
6. E. S. Kooij and B. Poelsema, "Shape and size effects in the optical properties of metallic nanorods," Phys. Chem. Chem. Phys. **8**, 3349–3357 (2006).
7. S. W. Prescott and P. Mulvaney, "Gold nanorod extinction spectra," J. Appl. Phys. **99**, 123504 (2006).
8. B. N. Khlebtsov and N. G. Khlebtsov, "Multipole plasmons on metal nanorods: scaling properties and dependence on particle size, shape, orientation, and dielectric environment," J. Phys. Chem. C **111**, 11516–11527 (2007).
9. W. Ni, X. Kou, and J. Wang, "Tailoring longitudinal surface plasmon wavelengths, scattering and absorption cross sections of gold nanorods," ACS Nano **2**, 677–686 (2008).
10. P. K. Jain, S. Eustis, and M. A. El-Sayed, "Plasmon coupling in nanorod assemblies: optical absorption, discrete di-

pole approximation simulation, and exciton-coupling model," J. Phys. Chem. B **110**, 18243–18253 (2006).
11. B. Willingham, D. W. Brandl, and P. Nordlander, "Plasmon hybridization in nanorod dimers," Appl. Phys. B: Lasers Opt. **93**, 209–216 (2008).
12. A. M. Funston, C. Novo, T. J. Davis, and P. Mulvaney, "Plasmon coupling of gold nanorods at short distances and in different geomteries," Nano Lett. **9**, 1651–1658 (2009).
13. S.-D. Liu and M.-T. Cheng, "Linear plasmon ruler with tunable measurement range and sensitivity," J. Appl. Phys. **108**, 034313 (2010).
14. E. J. Smythe, E. Cubukcu, and F. Capasso, "Optical properties of surface plasmon resonances of coupled metallic nanorods," Opt. Express **15**, 7439–7447 (2007).
15. P. R. Evans, R. Kullock, W. R. Hendren, R. Atkinson, R. J. Pollard, and L. M. Eng, "Optical transmission properties and elecric field distribution of interacting 2D silver nanorod arrays," Adv. Funct. Mater. **18**, 1075–1079 (2008).
16. C. Tserkezis, N. Papanikolaou, E. Almpanis, and N. Stefanou, "Tailoring plasmons with metallic nanorod arrays," Phys. Rev. B **80**, 125124 (2009).
17. R. Atkinson, W. R. Hendren, G. A. Wurtz, W. Dickson, A. V. Zayats, P. Evans, and R. J. Pollard, "Anisotropic optical properties of arrays of gold nanorods embedded in alumina," Phys. Rev. B **73**, 235402 (2006).
18. W. Dickson, G. A. Wurtz, P. Evans, D. O'Connor, R. Atkinson, R. Pollard, and A. V. Zayats, "Dielectric-loaded plasmonic nanoantenna arrays: a metamaterial with tuneable optical properties," Phys. Rev. B **76**, 115411 (2007).
19. M. Fleischer, D. Zhang, K. Braun, S. Jäger, R. Ehlich, M. Häffner, C. Stanciu, J. K. H. Hörber, A. J. Meixner, and D. P. Kern, "Tailoring gold nanostructures for near-field optical applications," Nanotecnology **21**, 065301 (2010).
20. D. J. Lipomi, M. A. Kats, P. Kim, S. H. Kang, J. Aizenberg, F. Capasso, and G. M. Whitesides, "Fabrication and replication of arrays of single- or multicomponent nanostructures by replica molding and mechanical sectioning," ACS Nano **4**, 4017–4026 (2010).
21. Y. Liu, J. Fan, Y.-P. Zhao, S. Shanmukh, and R. A. Dluhy, "Angle dependent surface enhanced Raman scattering obtained from an Ag nanorod array substrate," Appl. Phys. Lett. **89**, 173134 (2006).
22. A. V. Kabashin, P. Evans, S. Pastkovsky, W. Hendren, G. A. Wurtz, R. Atkinson, R. Pollard, V. A. Podolskiy, and A. V. Zayats, "Plasmonic nanorod metamaterial for biosensing," Nature Mater. **8**, 867–871 (2009).
23. G. A. Wurtz, W. Dickson, D. O'Connor, R. Atkinson, W. Hendren, P. Evans, R. Pollard, and A. V. Zayats, "Guided plasmonic modes in nanorod assemblies: strong electromagnetic couping regime," Opt. Express **16**, 7460–7470 (2008).
24. D. P. Lyvers, J.-M. Moon, A. V. Kildishev, V. M. Shalaev, and A. Wei, "Gold nanorod arrays as plasmonic cavity resonators," ACS Nano **2**, 2569–2576 (2008).
25. R. Kullock, W. R. Hendren, A. Hille, S. Grafström, P. R. Evans, R. J. Pollard, R. Atkinson, and L. M. Eng, "Polarization conversion through collective surface plasmons in metallic nanorod arrays," Opt. Express **16**, 21671–21681 (2008).
26. W. T. Lu and S. Sridhar, "Superlens imaging theory for anisotropic nanostructured metamaterials with broadband all-angle negative refraction," Phys. Rev. B **77**, 233101 (2008).
27. J. Yao, Z. Liu, Y. Liu, Y. Wang, C. Sun, G. Bartal, A. M. Stacy, and X. Zhang, "Optical negative refraction in bulk metamaterials of nanowires," Science **321**, 930 (2008).
28. Y. Liu, G. Bartal, and X. Zhang, "All-angle negative refraction and imaging in a bulk medium made of metallic nanowires in the visible region," Opt. Express **16**, 15439–15448 (2008).
29. A. Ono, J.-I. Kato, and S. Kawata, "Subwavelength optical imaging through a metallic nanorod array," Phys. Rev. Lett. **95**, 267407 (2005).
30. S. Kawata, A. Ono, and P. Verma, "Subwavelength colour imaging with a metallic nanolens," Nat. Photonics **2**, 438–442 (2008).
31. N. Stefanou, V. Yannopapas, and A. Modinos, "Heterostructures of photonic crystals: frequency bands and transmission coefficients," Comput. Phys. Commun. **113**, 49–77 (1998).
32. N. Stefanou, V. Yannopapas, and A. Modinos, "MULTEM2: a new version of the program for transmission and band-structure calculations of photonic crystals," Comput. Phys. Commun. **132**, 189–196 (2000).
33. G. Gantzounis and N. Stefanou, "Layer-multiple-scattering method for photonic crystals of nonspherical particles," Phys. Rev. B **73**, 035115 (2006).
34. C. Tserkezis and N. Stefanou, "Retrieving local effective costitutive parameters for anisotropic photonic crystals," Phys. Rev. B **81**, 115112 (2010).
35. M. I. Mishchenko, L. D. Travis, and A. A. Lacis, *Scattering, Absorption, and Emission of Light by Small Particles* (Cambridge University Press, 2002).
36. N. Stefanou, N. Papanikolaou, and C. Tserkezis, "Plasmonic nanostructures and optical metamaterials: studies by the layer-multiple-scattering method," Physica B **405**, 2967–2971 (2010).
37. N. W. Ashcroft and N. D. Mermin, *Solid State Physics* (Saunders, 1976).
38. J. F. Cornwell, *Group Theory in Physics*, Vol. 1 (Academic, 1984).
39. G. Gantzounis and N. Stefanou, "Theoretical analysis of three-dimensional polaritonic photonic crystals," Phys. Rev. B **72**, 075107 (2005).
40. L. D. Landau and E. M. Lifshitz, *Electrodynamics of Continuous Media* (Pergamon, 1960).
41. D. R. Smith, S. Schultz, P. Markoš, and C. M. Soukoulis, "Determination of effective permittivity and permeability of metamaterials from reflection and transmission coefficients," Phys. Rev. B **65**, 195104 (2002).
42. Th. Koschny, P. Markoš, E. N. Economou, D. R. Smith, D. C. Vier, and C. M. Soukoulis, "Impact of inherent periodic structure on effective medium description of left-handed and related metamaterials," Phys. Rev. B **71**, 245105 (2005).
43. C. Menzel, C. Rockstuhl, T. Paul, F. Lederer, and T. Pertsch, "Retrieving effective parameters for metamaterials at oblique incidence," Phys. Rev. B **77**, 195328 (2008).
44. J. Kanungo and J. Schilling, "Experimental determination of the principal dielectric functions in silver nanowire metamaterials," Appl. Phys. Lett. **97**, 021903 (2010).
45. C. R. Simovski and S. A. Tretyakov, "Local constitutive parameters of metamaterials from an effective-medium perspective," Phys. Rev. B **75**, 195111 (2007).
46. C. Menzel, T. Paul, C. Rockstuhl, T. Pertsch, S. Tretyakov, and F. Lederer, "Validity of effective material parameters for optical fishnet metamaterials," Phys. Rev. B **81**, 035320 (2010).
47. F. Abelès, Y. Borensztein, and T. López-Rios, "Optical properties of discontinuous thin films and rough surfaces of silver," Festkörperprobleme—Adv. Solid St. Phys. **24**, 93–117 (1984).
48. C. F. Bohren and D. R. Huffman, *Absorption and Scattering of Light by Small Particles* (Wiley, 1983).
49. F. L. Galeener, "Submicroscopic-void resonance: the effect of internal roughness on optical absorption," Phys. Rev. Lett. **27**, 421–423 (1971).
50. R. W. Cohen, G. D. Cody, M. D. Coutts, and B. Abeles, "Optical properties of granular silver and gild films," Phys. Rev. B **8**, 3689–3703 (1973).
51. R. Kullock, S. Grafström, P. R. Evans, R. J. Pollard, and L. M. Eng, "Metallic nanorod arrays: negative refraction and optical properties explained by retarded dipolar interactions," J. Opt. Soc. Am. B **27**, 1819–1827 (2010).
52. D. R. Smith and D. Schurig, "Electromagnetic wave propagation in media with indefinite permittivity and permeability tensors," Phys. Rev. Lett. **90**, 077405 (2003).
53. I. V. Lindell, S. A. Tretyakov, K. I. Nikoskinen, and S. Ilvonen, "BW media—media with negative parameters, capable of supporting backward waves," Microwave Opt. Technol. Lett. **31**, 129–133 (2001).
54. D. R. Smith, D. Schurig, J. J. Mock, P. Kolinko, and P. Rye, "Partial focusing of radiation by a slab of indefinite media,"

Appl. Phys. Lett. **84**, 2244–2246 (2004).
55. J. Schilling, "Uniaxial metallo-dielectric metamaterials with scalar positive permeability," Phys. Rev. E **74**, 046618 (2006).
56. C. Luo, S. G. Johnson, J. D. Joannopoulos, and J. B. Pendry, "All-angle negative refraction without negative effective index," Phys. Rev. B **65**, 201104(R) (2002).
57. H. Kosaka, T. Kawashima, A. Tomita, M. Notomi, T. Tamamura, T. Sato, and S. Kawakami, "Self-collimating phenomena in photonic crystals," Appl. Phys. Lett. **74**, 1212–1214 (1999).
58. D. N. Chigrin, S. Enoch, C. M. Sotomayor Torres, and G. Tayeb, "Self-guiding in two-dimesional photonic crystals," Opt. Express **11**, 1203–1211 (2003).
59. R. Iliew, C. Etrich, and F. Lederer, "Self-collimation of light in three-dimensional photonic crystals," Opt. Express **13**, 7076–7085 (2005).
60. J. Shi, B. K. Juluri, S.-C. S. Lin, M. Lu, T. Gao, and T. J. Huang, "Photonic crystal composites-based wide-band optical collimator," J. Appl. Phys. **108**, 043514 (2010).
61. D. W. Prather, S. Shi, J. Murakowski, G. J. Schneider, A. Sharkawy, C. Chen, B. L. Miao, and R. Martin, "Self-collimation in photonic crystal structures: a new paradigm for applications and device development," J. Phys. D: Appl. Phys. **40**, 2635–2651 (2007).
62. C. Luo, S. G. Johnson, J. D. Joannopoulos, and J. B. Pendry, "Subwavelength imaging in photonic crystals," Phys. Rev. B **68**, 045115 (2003).